2024 IEEE International Conference on Robotics and Automation (ICRA 2024)
May 13-17, 2024. Yokohama, Japan

Optimization of Flexible Bronchoscopy Shape Sensing Using Fiber Optic Sensors

Xinran Liu, Hao Chen and Hongbin Liu*

Abstract— **This work presents a novel shape evaluation and optimization approach for shape sensing, specifically targeting the constrained, irregular, and intricate spatial shapes of flexible bronchoscopes (FB) in human bronchial tree. The proposed evaluation criteria and optimization methods combine clinical significance related to bronchial anatomical structures and address issues related to singular points and discontinuities in traditional shape reconstruction models. Three-dimensional experiments were conducted within eight spatial complex configurations printed from a proportional bronchial model. The 3D experiment results demonstrate an average reduction of approximately 34.1% in shape reconstruction errors across all eight airway models compared to the traditional model, validating the effectiveness and feasibility.**

I. Introduction

According to a survey conducted in 2020 by the American Cancer Society [1], the mortality rate for lung and bronchus cancer stands at a staggering 38.5 per 100,000 individuals annually. In recent times, the field of robot-assisted minimally invasive surgery (MIS) with flexible bronchoscopy (FB) has emerged as a revolutionary technology in the early screening, diagnosis, and treatment of lung and bronchial cancer. This advancement has contributed significantly to reducing mortality rates associated with these diseases in clinical practice. However, the bronchial tree exhibits a multi-level tree structure, along with characteristics such as elongation, curvature, and peristalsis, posing significant challenges for the precise control and navigation of the FB robot system. To ensure the protection of vulnerable areas, and facilitate optimal diagnostic and therapeutic interventions, the accurate sense of the FB shape becomes indispensable within the realm of surgical procedures [2].

In comparison to other shape-sensing traditional methods, such as electromagnetic (EM) tracking, image-based tracking, and tendon-driven models [3][4], fiber optic sensors (FOSS) present a highly effective alternative due to several distinct advantages, including immunity to electromagnetic interference (EMI), absence of ionizing radiation, strong embedding capability, lightweight and flexible characteristics, making fiber optic sensors particularly well-suited for integration into FB used in MIS [5][6]. Without the requirement for visual contact or models, FOSS can be attached to the substrate to measure, thus, allowing for safe, continuous, dynamic, and direct shape sensing [7]-[10].

The shape-sensing approach based on FOSS typically relies on measuring strains along the fiber's length using quasi-distributed sensing methods, including Fiber Bragg Grating (FBG), or distributed sensing methods such as Rayleigh scattering-based and Brillouin scattering-based techniques [11][12]. The basic model for reconstructing shape is grounded in differential geometry and involves the integration of discrete strain measurements. This approach is relatively straightforward to implement and yields high accuracy when applied to objects within unconstrained open environments, characterized by high rigidity and minor bending deformations.

However, challenges arise due to the intricate nature of the human bronchial tree, which consists of narrow, multi-layered branching structures (typically subdivided into 24 levels). In this environment, low-rigidity FBs often exhibit significant bending deformations, resulting in constrained, irregular, and complex spatial shapes. These challenges pose difficulties in achieving accurate shape reconstruction modeling and meeting the clinical requirements for target precision [13].

When it comes to longer FBs, it is difficult to directly avoid and eliminate errors in curvature measurement during integrating process, nevertheless, cumulative errors exhibit non-uniform distribution across various anatomical locations. In clinical practice, it is imperative to acknowledge that not all anatomical sites hold equal significance in terms of shape accuracy assessment. Specifically, the precision of shape reconstruction at the endpoint holds paramount importance, as it directly influences the successful navigation into the bronchiolar branch and the effectiveness of examination and therapeutic interventions within specific regions. Furthermore, the contact points with the bronchial mucosa and bending points are directly related to the degree of trauma to the patient's airway and the subsequent path of maneuvering the FB [14].

However, to the best of our knowledge, all current assessments of shape accuracy are based on traditional Euclidean distance methods, which have limitations [15]:

1) Insensitivity to non-rigid transformations of FB shapes.
2) Potential oversight of the aforementioned critical points.
3) Inability to discern similarity and consistency in local and global shape variations.

This work was supported by the Institute of Automation, Chinese Academy of Sciences, Kings College London and the InnoHK programme. (Corresponding author: Hongbin Liu).

X. Liu, H. Chen is now with the School of Artificial Intelligence, University of Chinese Academy of Sciences, Beijing 100049, China, and also with the State Key Laboratory of Multimodal Artificial Intelligence Systems, Institute of Automation, Chinese Academy of Sciences Beijing 100190, China (e-mail: liuxinran2020@ia.ac.cn; chen.hao2020@ia.ac.cn).

H. Liu is a Professor at Chinese Academy of Sciences, Institute of Automation (CASIA), Executive Director for the Centre of AI and Robotics (CAIR), Hong Kong Institute of Science & Innovation, Chinese Academy of Sciences. He is also an adjunct Reader and director of the Haptic Mechatronics and Medical Robotics (HaMMeR) lab at the School of Biomedical Engineering and Imaging Sciences, King's College London (KCL), UK. (e-mail: liuhongbin@ia.ac.cn).

These limitations render traditional Euclidean distance metrics not entirely effective in accurately reflecting the practical application outcomes during clinical operations. For instance, three FB shapes, all exhibiting the same average normalized Euclidean distance when compared to the true shape ("Ground Truth" in red), are depicted as Fig.1. S1 can provide accurate navigation and effective treatment. However, S2 experiences airway perforation at the branching point, and S3, while closely resembling the true shape at the front end, enters the wrong branch towards the end. Both S2 and S3 are considered medical accidents [14].

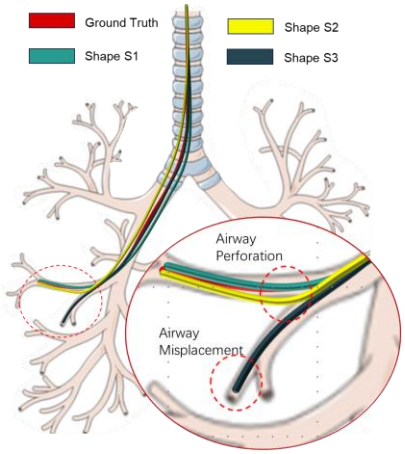

Fig.1 Three different shapes within the bronchus under the evaluation of Euclidean distance.

Therefore, in this paper, we propose a novel shape evaluation criterion that incorporates the significance of the bronchial anatomy structure. In this evaluation criterion, the points with greater significance in terms of precision and system safety are considered as shape key points. Based on this, addressing the inherent drawbacks of several studied shape reconstruction models (Frenet-Serret frame [13], Bishop frame [16], Beta frame [17]), such as:

1) The Frenet-Serret frame's susceptibility to singularities when the curve changes direction and its discontinuity in the presence of a local line [18][19].

2) The Bishop frame lacks the presence of the principal normal vector.

3) The complexity of calculations in the Beta frame method due to additional vectors and equations while addressing situations where the Frenet-Serret method falls short.

We propose a fusion model based on the Frenet-Serret frame and Beta frame to optimize shape reconstruction. Compared to the state-of-the-art geometric shape reconstruction model, the proposed fusion model resolves issues related to jump discontinuities arising from curve changes in concavity and undefined points of zero curvature, which are defined as optimizable points in our model. Another advantage of our proposed fusion model is that it does not introduce extra computational complexity and exhibits strong generality and scalability when dealing with intricate spatial shapes. A set of 3D experiments are performed in channels printed from a proportional bronchial model.

The rest of this work is organized as follows: Section II delves into the FB shape sensing scheme, covering sensor design and shape reconstruction modeling. Section III addresses the challenges in shape reconstruction and details the newly proposed evaluation criterion and fusion optimization model. Section IV details the experiments conducted on an equal scaled bronchial model to validate the proposed approach. Section V provides a summary of the research contributions and significance.

II. Sensor Design and Shape Modeling

A. Shape sensor scheme

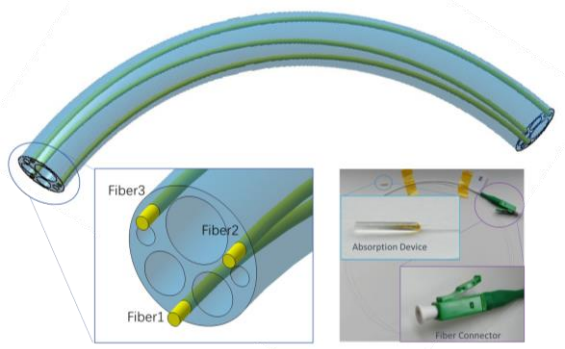

Fig.2 Design Scheme for FB: Three FOSS were installed and bonded within three separate channels using epoxy resin adhesive. These three fiber channels were equally spaced at an angle of 120°. Detailed section configurations are provided in TABLE I.

TABLE I Configuration of Multi-Channel

Label	Diameter (mm)	Numbers	Channel function	Note
1	1.37	1	Instruments	Forceps etc.
2	0.90	2	Sensors	CCD, LED etc.
3	0.41	2	Reserved	-
4	0.28	3	Optical fibers	Shape sensing

As shown in Fig.2 and TABLE I, the FB scheme with shape sensing is designed, which uses multiple channels to integrate various components, including surgical tools (e.g., biopsy forceps), CCD image sensors, and light sources.

To ensure the safety and accuracy of the surgery, the FB needs to provide stable bending control and elastic recovery capabilities. Therefore, this paper utilizes PEBAX 6333, a commonly used biocompatible material in clinical medicine, for the design. This material offers sufficient bending elasticity and stability, enabling it to withstand significant bending loads and rapidly recover its shape after deformation. Based on anatomical data of human bronchial lumens and considering the requirements of MIS and the dimensions of commonly used ultrathin bronchoscopes (such as the BF-XP160F; Olympus Medical, Tokyo, Japan) [19], the FB was designed with a diameter of 2.84mm and a total length of 500mm. Additionally, to ensure the measurement of FOSS exhibits good strain linearity and a wide dynamic measurement range, a certain degree of pre-loading strain is required during the insertion and bonding of FOSS.

B. Curvature-Strain Model

For strain sensitivity, bending resistance, and installation precision, optical fibers with a polyimide coating (diameter of 155μm±5μm) were chosen. The channel diameter was set at 280μm to ensure a smooth pathway for the optical fibers and to facilitate a robust bond between the fibers and the channels.

Fig. 3. represents a schematic of the FB cross-section channel layout and optical fiber arrangement.

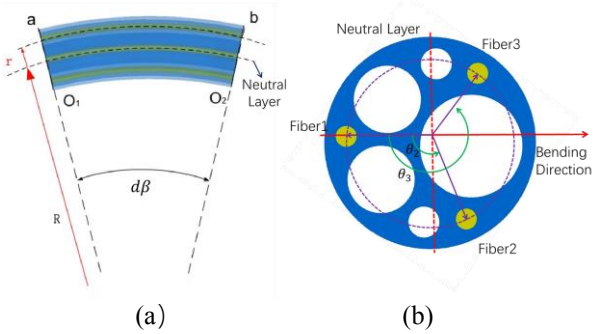

(a) (b)

Fig.3(a) a section of a micro-segment. The central angle corresponding to the bending is $d\beta$, the bending radius is R, and the distance between the optical fiber and the neutral axis of the FB is $r = 1.126mm$. (b) The angular layout relationship of sensing fiber in any microsection.

Fig.3(a) utilizes the mathematical theory's differential element method for shape analysis by extracting small cross-sectional segments. In this theoretical derivation, the term "micro-segment" is a continuous mathematical tool for analysis and does not represent actual measurement points. The formula for the normal strain of ab corresponding to the outermost optical fiber is:

$$\varepsilon = \frac{\text{ab-dx}}{\text{dx}} = \frac{\text{(R+r)d}\beta\text{-Rd}\beta}{\text{Rd}\beta} = \frac{\text{r}}{\text{R}} \tag{1}$$

Where ε is the strain generated by the optical fiber when the FB is bent, ab is the extension length when it is stretched outside, $dx = O_1O_2$ is the bending length on the neutral layer of the microsegment, $d\beta$is the central angle corresponding to the microsegment bending in space, and r is the distance from the fiber core to the neutral axis.

Based on the Euler-Bernoulli beam theory, the FB can be approximated as an ideal elastic rod exhibiting uniform, linear elastic, incompressible, and isotropic behavior due to characteristics such as high slenderness ratio, negligible cross-sectional deformations, and longitudinal stretching capabilities. Under these reasonable assumptions, a length-invariant layer known as the neutral layer exists along the axis direction. During the surgical procedure, when the FB bends downward, the fibers in the upper part of the neutral layer experience tensile stress along the axis, while the fibers in the lower part experience compressive stress along the axis.

In order to simplify the shape sensing model and calibration process, three optical fibers (designated as Fiber1, Fiber2, and Fiber3) are evenly positioned at angle of 0°, 120°, and 240°.

$$\begin{cases} \varepsilon_1 = \varepsilon_{max}\cos(\varphi_m) + \varepsilon_0 \\ \varepsilon_2 = \varepsilon_{max}\cos(\varphi_m + 120°) + \varepsilon_0 \\ \varepsilon_3 = \varepsilon_{max}\cos(\varphi_m + 240°) + \varepsilon_0 \end{cases} \tag{2}$$

Where ε_0 is the strain offset contributed by the temperature change and axial force of FB, which is a system error related to the testing conditions and can be mitigated through data analysis of measurements

$\varepsilon_{max} = \frac{r}{R} = k \cdot r$, r is the distance from the fiber to the neutral axis and k is the curvature of FB.

C. *Shape reconstruction method*

According to the principles of differential geometry and the Frenet-Serret frame, the geometric properties of a spatial curve can be described by three orthogonal vectors formed at each point: the tangent vector ($\vec{T}$), the normal vector ($\vec{N}$), and the binormal vector ($\vec{B}$). The curvature and torsion of each microsegment are related to the TNB vectors as expressed in (3).

$$\begin{cases} \nabla\vec{T}_m = \|\vec{k}_m\|\vec{N}_m \\ \nabla\vec{N}_m = -\|\vec{k}_m\|\vec{T}_m + \tau_m\vec{B}_m \\ \nabla\vec{B}_m = -\tau_m\vec{N}_m \\ \nabla\vec{r}_m = \vec{T}_m \end{cases} \tag{3}$$

Where $\vec{\text{k}}_\text{m}$ represents the spatial curvature of each microsegment along the FB neutral axis, and $\|\vec{k}_m\|$ represents the modulus of the corresponding spatial curvature. τ_m indicates the torsion of the corresponding microsegment node. Moreover, $\vec{T}_m$ and $\vec{\text{N}}_\text{m}$ refer to the tangent and normal vectors, respectively, at the m-th microsegment node. Additionally, $\vec{\text{B}}_\text{m}$ denotes the cross product of $\vec{\text{N}}_\text{m}$ and $\vec{T}_m$ at the m-th microsegment node, and $\vec{\text{r}}_\text{m}$ represents the natural coordinate at this microsegment node.

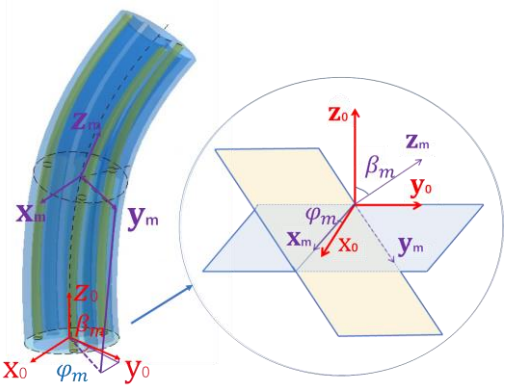

Fig.4 The geometric relationship of the m-th microsegment. Here, β_m represents the spatial bending angle of the m-th microsegment relative to the initial coordinate system of FB, whereas φ_m represents the twisting angle of the m-th microsegment in the XOY plane projection of the initial coordinate system.

The global coordinate system of the FB is established in this paper with the initial state oriented vertically upward, where the axis serves as the Z-axis, and the positive bending direction of the first microsegment of Fiber1 is defined as the Y-axis. This is shown in the Fig.4.

As the curvature direction of a point on the curve is perpendicular to the tangent direction at that point, the axial strain of each fiber on the FB can be computed using (1), thereby determining the apparent strain of the FB.

$$\vec{\varepsilon}_{FB,m} = \frac{1}{3}\sum_i^3 \varepsilon_{\text{i,m}}(\sin\beta_\text{m} \cdot \vec{i} + \cos\beta_\text{m} \cdot \vec{j}) \tag{4}$$

Where, $\varepsilon_{i,m}$ represents the axial strain of the *i-th* fiber at the *m-th* microsegment. β_m is referred to as the bending angle of the *m-th* microsegment, which refers to the angle between the tangent vector of the microsegment and the

XOY plane of the global coordinate system. $\vec{i}$ and $\vec{j}$ are unit vectors on the x+ and y+ axes, respectively.

According to the relative position and curvature of the optical fibers, the apparent curvature, bending angle, and torsion of the FB can be calculated as follows:

$$\begin{cases} \vec{k}_{FB,m} = \frac{1}{r}\vec{\varepsilon}_{FB,m} \\ \varphi_m = arctan\frac{\vec{k}_{FB,m}\cdot\vec{j}}{\vec{k}_{FB,m}\cdot\vec{i}} \\ \tau_m = \nabla\varphi_m \end{cases} \quad (5)$$

where $\vec{k}_{FB,m}$, φ_m, and τ_m represents the spatial curvature, twsit angle, and torsion of the *m-th* microsegment of the neutral axis, respectively. r signifies the distance between the *i-th* fiber and the neutral axis (r=1.126mm, in this paper).

The boundary conditions for (2) are $\vec{r}_{FB,0} = (0,0,0), \vec{k}_{FB,0} = (0,0), \tau_0 = 0$. The resultant shape can be iteratively calculated using the triplet vectors $\vec{T}_{FB,m}$, $\vec{N}_{FB,m}$, and $\vec{B}_{FB,m}$, along with $\vec{r}_{FB,m}$ for each microsegment. In the specific experiment, a total of 188 sensor nodes are involved in the iterative calculation process, a quantity determined based on the spatial resolution of the distributed strain interrogator and the length of the FB.

III. Fusion Evaluation Based on Endpoint and Key Points

A. Fusion Evaluation Based on Endpoint and Key Points

The conventional method for assessing shape accuracy relies on comparing the reconstruction shape with ground truth using the Euclidean distance to quantify errors. Specifically, in the context of shape sensing for flexible instruments, most researchers normalize the Euclidean distance errors between sensing nodes and their corresponding ground truth points to characterize their effectiveness [21][22].

Define the spatial coordinates of each sensing node obtained through the shape reconstruction model are $P_i^C(x_i^C, y_i^C, z_i^C)$, and their corresponding ground truth shape coordinates are $P_i^T(x_i^T, y_i^T, z_i^T)$, thus the Euclidean distance for each sensing node can be expressed as follows:

$$D_i = \sqrt{(x_i^C - x_i^T)^2 + (y_i^C - y_i^T)^2 + (z_i^C - z_i^T)^2} \quad (6)$$

where D_i represents the Euclidean distance for the i-th sensing node.

Subsequently, we calculate the average of the normalized distances for all sensing nodes to serve as the evaluation metric for the overall shape reconstruction:

$$\bar{d} = \frac{1}{N}\sum_{i=1}^{N}\frac{D_i}{D_{max}} \quad (7)$$

Where D_{max} represents the maximum Euclidean distance among all sensing nodes, and d_i represents the normalized distance for the i-th sensing node.

In the conventional method, the average normalized Euclidean distance is computed through linear averaging, assigning equal weights to FB nodes ($\omega_i^{Gen} = 1/N$). However, this method for assessing shape quality has limitations, as it tends to overlook key points, lacks sensitivity to deformations, and relies on a simplistic normalized distance, restricting its comprehensive assessment in practical applications.

In order to effectively characterize points with greater significance in terms of precision and system safety, "Shape key points" are defined to encompass mucosal contact points and bending points. These can be summarized as follows: $Keypoints = \{(k,\tau)|k = 0 \vee \frac{dk}{ds} = 0 \vee \frac{d\tau}{ds} = 0)\}$. Both "Shape key points" and "Endpoint" are considered to be points of significant importance on the entire FB that warrant close attention. Thus, a novel evaluation method based on FB endpoints and key shape points are proposed as below.

Suppose that the endpoint of FB shape reconstruction is denoted as P_{End}^C, and the set of K shape key points is represented as P_{Key}^C=$[P_1^C, \cdots, P_K^C]$.

The weight space for each node in FB is given as follows:

$$\Psi^C=[\omega_{End}^C, \omega_{Key}^C, \omega_{Con}^C] \quad (8)$$

Where ω_{End}^C represents the weight for the endpoint, ω_{Key}^C denotes the weights for K shape key nodes, and ω_{Con}^C corresponds to the weight for FB's conventional nodes. The conventional node weights are determined using a linear averaging method, with the number of conventional nodes equal to $N-(K+1)$.

$$\begin{cases} \omega_{End}^C = a, & a \in (0,1) \\ \omega_{Key}^C = \begin{cases} b, & b \in \left(0, \frac{1-a}{K}\right), 0 < K < N-1 \\ 0, & K = 0 \end{cases} \\ \omega_{Con}^C = \frac{1-a-Kb}{M}, & M = N-(K+1), N > 0 \end{cases} \quad (9)$$

Where a represents the evaluation weight for the FB endpoint, and b stands for the evaluation weight of shape key points.

Therefore, the fusion evaluation metric based on flexible bronchoscope endpoint and shape key points is as follows.

$$\bar{d}^C = \frac{1}{M}\sum_{i=1}^{M}\omega_{Con}^C \cdot d_i + \frac{1}{K}\sum_{j=1}^{K}\omega_{Key}^C \cdot d_j + \omega_{End}^C \cdot d_N \quad (10)$$

B. Fusion Optimization Model for Reconstruction

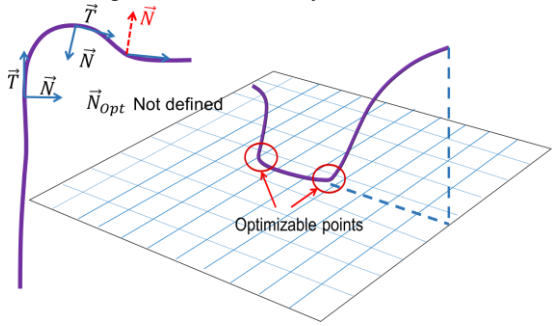

Fig.5 Undefined points of zero curvature and points of jump discontinuities arising from curve changes in concavity in the Frenet-Serret frame.

The most commonly employed shape reconstruction method presently is based on the Frenet-Serret Frame, which converts distributed curvature measurements into a three-dimensional shape by combining elastic rod theory and differential geometry. However, it has limitations as it requires the curve to be at least thrice differentiable. Additionally, it is undefined at those points where the

curvature is zero and has a jump discontinuity where curve changes concavity.

In the complex branching bronchial environments discussed in this paper, the FB is prone to experiencing curvature discontinuities and noticeable shifts in the normal direction [23][24]. These factors lead to the occurrence of computational singularities, resulting in shape reconstruction errors, as depicted in Fig. 5.

To address the primary drawback of the Frenet-Serret frame, in the proposed optimization model, "optimizable points" are defined as points falling into the following three cases: 1) Local line segments, i.e., points where the curvature is zero. 2)Points where the normal vector experiences discontinuous jumps due to chanv ges in the curvature's concavity. 3)Singular points that arise when local curves do not satisfy thrice differentiability completely.

The Beta frame is a curve parameterization method that provides a continuous description of curve properties, effectively overcome specific limitations of the normal vector discontinuities seen in traditional Frenet-Serret frames [15].

Specifically, the Beta frame employs a relatively parallel vector field, denoted as $\vec{M}_m$, which remains continuous along the curve and satisfies $\vec{M}_m = g_m \vec{T}_m$, where g_m is a function, and $\vec{T}_m$ is the tangent vector of the curve in the Frenet-Serret frame. By selecting an initial unit normal vector $\vec{M}_0$, an orthogonal frame $\{\vec{T}, \vec{M}_1, \vec{M}_2\}$ can be generated. $\vec{T}$ represents the tangent vector, indicating the direction of the curve. $\vec{M}_1$ and $\vec{M}_2$ are two vectors orthogonal to the tangent vector, representing the normal vector and binormal vector of the curve, respectively. Initial conditions:

1) If the curve is planar, then $\vec{M}_{1,0} = \vec{N}_0$, and $\vec{M}_{2,0} = \vec{T}_0 \times \vec{N}_0$.

2) If the curve is non-planar, then $\vec{M}_{1,0} = \vec{N}_0$, and $\vec{M}_{2,0} = \vec{B}_0$.

Therefore, the correspondence between the Beta frame and the Frenet-Serret frame is as follows:

$$\vec{T}_m^B = \vec{T}_m \tag{11}$$

The auxiliary normal vector $\vec{B}_m^B$ of the Beta frame can be represented as the cross product of the tangent vector $\vec{T}_m$ in the Frenet-Serret frame and the normal vector $\vec{N}_m^B$ in the Beta frame.

$$\vec{B}_m^B = -sin(\theta_m)\,\vec{M}_{1,m} + \cos(\theta_m)\,\vec{M}_{2,m} \tag{12}$$

Here, θ_m indicates the direction of the vector field. In the Beta frame, the principal normal vector N_m^B is defined as:

$$\vec{N}_m^B = -\vec{M}_m \tag{13}$$

Rather than the $\vec{N}_m$ in the Frenet-Serret frame

In the Beta frame, the principal normal vector $\vec{N}_m^B$ remains continuous, resolving the problem of normal vector discontinuity encountered in the traditional Frenet-Serret frame. Therefore, the adoption of the Beta frame enables us to surpass the limitations of the Frenet-Serret frame.

However, the Beta frame method has the following limitations:1) Introduction of $\vec{M}_m$ and trigonometric functions, along with additional vector operations, complicates calculations compared to the traditional Frenet-Serret frame. 2) Calculations in the Beta frame are sensitive to initial conditions, such as the choice of $\vec{M}_0$ and θ_0, which may lead to significant errors.

In practical shape reconstruction, correcting and compensating optical fiber strain data, computing apparent curvature, and solving curvature and torsion for each sensor node help assess if nodes meet Frenet-Serret framework requirements. Subsequently, fusion optimization with the Beta frame method can be performed.

Assuming the curve's normal vector remains continuous, and its polar coordinates are represented as (r, θ), where $r(0) = 0$, we have:

$$(\vec{M}_1, \vec{M}_2) = (rcos(\theta), rsin(\theta)) \tag{14}$$

Then, we can globally define $\vec{N}$ as follows:

$$\vec{N}_m = \vec{M}_{1,m}\cos(\theta_m) + \vec{M}_{2,m}\sin(\theta_m) \tag{15}$$

In this model, "optimizable points" encompass the previously mentioned "shape key points."

IV. EXPERIMENTAL RESULTS

A. Experimental system setup

The experimental setup consisted of an optical distributed sensor interrogator (LUNA OdiSI-6100), an FB shape sensor, and a computer for displaying results. The interrogator, based on OFDR technology, provided high spatial resolution strain measurements on three embedded optical fibers of the FB shape sensor. The sensor nodes were spaced at 2.6 mm intervals, with a dynamic strain range of -12000 $\mu\varepsilon$ to +12000 $\mu\varepsilon$ [25]. The measured data were transmitted to a computer for displaying shape sensor results through a TCPIP communication interface. The implementation of the algorithm was coded using Python.

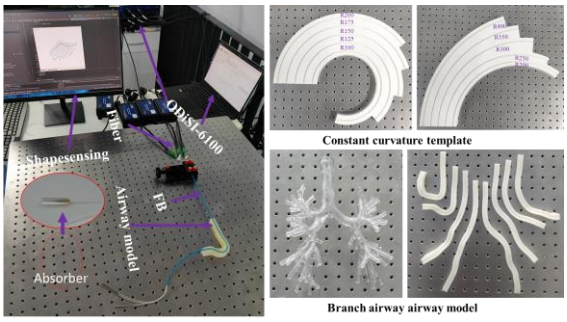

Fig.6 Experimental system

To calibrate FB sensing nodes, we used templates with radii from 100mm to 400mm. The process:

1) Secure FB's initial end with clamps.

2) Connect optical fibers to OdiSI-6100.

3) Insert FB into temp lates with R=100mm to R=400mm.

4) Measure strain $\varepsilon_{i,j}^{test}$ at effective nodes.

5) Calculate ε_i^{Theory} and establish an optimization problem to minimizes the cost function.

$$C(\Omega) = argmin \sum_{i=1}^{3} \left\| \varepsilon_i^{Theory} - \varepsilon_{i,j}^{test} \right\|_2^2 \tag{16}$$

6) In experiments, gradient descent with a learning rate of 0.1 was employed for sensitivity corrections over 188 iterations, matching the number of sensor nodes in FB. Convergence was set at a 20$\mu\varepsilon$ threshold.

B. Shape reconstruction based on bronchial models

During navigation in the airways, the FB does not precisely follow the median line due to its semi-rigid nature. However, in secondary bronchi and their subsequent branches, the FB is predominantly influenced by environmental constraints, resulting in a curvature profile closely resembling the central axis. To simulate the spatial morphology of the designed FB within the bronchial environment and acquire more accurate ground truth data, this study utilized a human bronchial digital model. Specifically, the central axes of two bronchial channels were selected within the left upper lobe, right upper lobe, left lower lobe, and right lower lobe. Three-dimensional airway models were established through 3D printing using 8200Pro resin, as depicted in Fig.7.

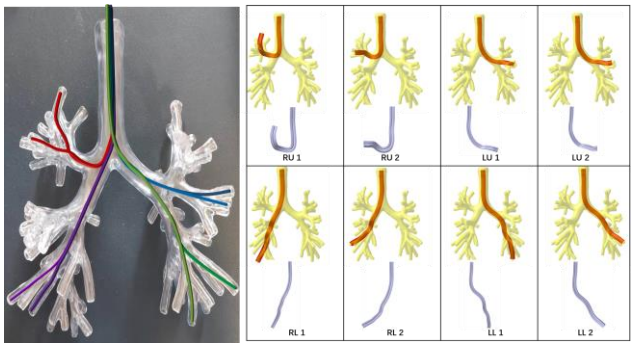

Fig.7 Bronchial model with 3D printed airway models.

In this experiment, the airway mold's diameter was designed to be 4mm to precisely accommodate the designed FB. The designed FB is bent into eight Spatial complex configurations. The 3D shape reconstruction results using both the traditional Frenet-Serret frame method and the proposed Fusion optimization model are shown in blue and yellow in Fig.8(a), respectively, utilizing the information provided by the FOSS. And the ground truth curve is displayed in red.

Under the evaluation of Euclidean distance, the error results for the two shape reconstruction models are presented in Fig.8(b). For each case, the shape reconstruction error of the traditional method is shown in blue, while the proposed method is depicted in green. The experimental results demonstrate that, compared to the traditional method, this approach achieved an average reduction of 34.1% in shape reconstruction errors across all eight airway models. It can be observed that the proposed optimization model significantly improves shape precision in various anatomical locations within the lung lobes. Given that the effective length of FB in different branches varies, the proportion of cumulative errors at different anatomical positions is also distinct.

In the proposed fusion evaluation criterion, as illustrated in Fig.8(c), the blue and green lines represent the error levels for the two methods, respectively. Normalization is applied to eliminate the cumulative error caused by varying lengths. The selected anatomical structures of the upper lobe airway exhibit greater complexity and curvature when compared to the lower lobe airway, featuring notable variations in both curvature and torsion. Throughout the airway navigation process in the upper lobe, clinicians face heightened challenges due to an increased number of contact points and turning points, particularly concerning airway selection and insertion control during MIS.

Fig. 8(c) illustrates that the implementation of the fusion algorithm leads to an overall reduction in the average normalized error of shape, with a more significant decrease evident in the upper lobe airway. This finding substantiates the guiding efficacy of the proposed evaluation method for intricate airway structures.

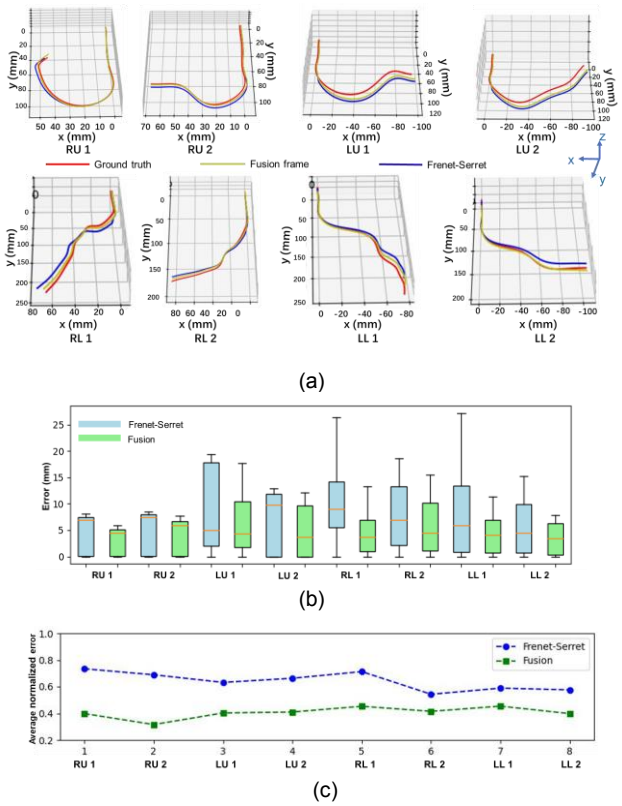

Fig.8 (a)Reconstruction shapes by the Frenet-Serret Frame and optimization model. (b)The comparison of errors in shape reconstruction between two methods under Euclidean distance evaluation criterion. (c)The comparison of errors in shape reconstruction between two methods under proposed Fusion evaluation criterion.

V. DISCUSSION AND CONCLUSION

In this work, addressing the constrained and intricate spatial morphology of flexible bronchoscopes in minimally invasive surgery, we have proposed an innovative evaluation and optimization model to achieve more precise three-dimensional shape perception. This approach, based on the clinical significance of different anatomical positions, enhances traditional shape reconstruction frameworks. Experimental results have demonstrated the effectiveness and scalability of this approach in complex spatial morphologies.

Future work will involve further research and validation of this approach on a substantial amount of clinical data and samples. The goal is to provide medical professionals with a practical, intelligent and meaningful shape sensing and navigation system[26].

REFERENCES

[1] Jemal A, Siegel R, Xu J, "Cancer statistics 2020", CA: A Cancer Journal Clinicians, Vol.70, ISS.1, Jan.2020, pp:277–300, DOI: 10.3322/caac.21590.

[2] Amirhosein Alian, Emilia Zari, Zeyu Wang, Enrico Franco, James P. Avery, Mark Runciman, Benny Lo, Ferdinando Rodriguez y Baena, and George Mylonas, "Current Engineering Developments for Robotic Systems in Flexible Endoscopy", Techniques and Innovations in Gastrointestinal Endoscopy, Vol.25, Issue 1, 2023, pp.67-81, DOI: 10.1016/j.tige.2022.11.006.

[3] N. J. Deaton, M. Sheft and J. P. Desai, "Towards FBG-Based Shape Sensing and Sensor Drift for a Steerable Needle", IEEE/ASME Transactions on Mechatronics, DOI: 10.1109/TMECH.2023.3239750.

[4] Jingpei Lu, Fei Liu, Cedric Girerd, Michael C. Yip, "Image-based Pose Estimation and Shape Reconstruction for Robot Manipulators and Soft, Continuum Robots via Differentiable Rendering", arXiv preprint arXiv:2302.14039. DOI:10.48550/arXiv.2302.14039

[5] Chengzhi Song, Xin Ma, Xianfeng Xia, Philip Wai Yan Chiu, Charing Ching Ning Chong, Zheng Li. "A robotic flexible endoscope with shared autonomy: a study of mockup cholecystectomy", Surg Endosc. Vol. 34(6), pp:2730-2741, Jun. 2020, PMID: 31722046, DOI: 10.1007/s00464-019-07241-8.

[6] Z. Liu, R. Li, Y. Cao, F. Feng and L. Xie, "Shape Sensing of a Soft Robot Using Fiber Bragg Gratings for Single-port Transvesical Radical Prostatectomy", IEEE International Conference on Robotics and Biomimetics (ROBIO), 2022, pp: 2087-2092, DOI: 10.1109/ROBIO55434.2022.10012004.

[7] Floris, Ignazio, et al. "Fiber Optic Shape Sensors: A Comprehensive Review", Optics and Lasers in Engineering, Vol. 139, 1 Apr. 2021, p. 106508, DOI:10.1016/j.optlaseng.2020.106508.

[8] R. J. Roesthuis, M. Kemp, J. J. van den Dobbelsteen, and S. Misra, "Three-dimensional needle shape reconstruction using an array of fiber Bragg grating sensors", IEEE/ASME Trans. Mechatronics, Vol. 19, No. 4, pp. 1115–1126, Aug. 2014, DOI: 10.1109/TMECH.2013.2269836.

[9] K. Song, D. A. Lezcano, G. Sun, J. Seob Kim, and I. I. Iordachita, "Towards automatic robotic calibration system for flexible needles with FBG sensors", Proc. Int. Symp. Med. Robot. (ISMR), Nov. 2021, pp:1–7, DOI: 10.1109/ISMR48346.2021.9661542.

[10] Jun Sheng, Nancy J. Deaton, and Jaydev P. Desai, "A Large-Deflection FBG Bending Sensor for SMA Bending Modules for Steerable Surgical Robots", IEEE Int. Conf. Robot. Automat., 2019, pp.900-906, DOI:10.1109/ICRA.2019.8794302.

[11] C. Xu and Z. Sharif Khodaei, "Shape Sensing with Rayleigh Backscattering Fibre Optic Sensor", Sensors, Vol. 20, No. 14, pp:4040-, Jul. 2020, DOI: 10.3390/s20144040.

[12] Omar Al-Ahmad, Mouloud Ourak, Jan Van Roosbroeck, Johan Vlekken, and Emmanuel Vander Poorten, "Improved FBG-Based Shape Sensing Methods for Vascular Catheterization Treatment", IEEE Robot. Automat. Lett., Vol. 5, No. 3, pp.4687-4694, July 2020, DOI: 10.1109/LRA.2020.3003291.

[13] J. Moore and M. Rogge, "Shape sensing using multi-core fiber optic cable and parametric curve solutions", Opt. Express, Vol.20, No. 3, pp:2967-2973, Jan. 2012.

[14] Tyler J. Paradis, Jennifer Dixon and Brandon H. Tieu, "The role of bronchoscopy in the diagnosis of airway disease", Journal of Thoracic Disease, 2016 Dec; 8(12): 3826–3837. Doi: 10.21037/jtd.2016.12.68.

[15] Xuan Thao Ha, Di Wu, Mouloud Ourak, Gianni Borghesan, Arianna Menciassi, and Emmanuel Vander Poorten, "Sensor Fusion for Shape Reconstruction Using Electromagnetic Tracking Sensors and Multi-Core Optical Fiber", IEEE Robot. Automat. Lett., Vol. 8, No. 7, pp.4076-4083, July 2023, DOI: 10.1109/LRA.2023.3280456.

[16] Jiwen Cui, Shiyuan Zhao, Chaoqiang Yang, and Jiubin Tan, "Parallel Transport Frame for Fiber Shape Sensing", IEEE Photonics Journal, Vol. 10, No. 1, February 2018, DOI: 10.1109/JPHOT.2017.2782736.

[17] Daniel Carroll, Emek K¨ose & Ivan Sterling, "Improving Frenet's Frame Using Bishop's Frame", Journal of Mathematics Research, Nov. 2013, DOI: 10.5539/jmr.v5n4p97.Source: arXV.

[18] Sonja Jäckle, Tim Eixmann, Hinnerk Schulz-Hildebrandt, Gereon Hüttmann & Torben Pätz, "Fiber optical shape sensing of flexible instruments for endovascular navigation", International Journal of Computer Assisted Radiology and Surgery, Sep. 2019, Vol. 14, pp.2137–2145, DOI:10.1007/s11548-019-02059-0.

[19] Phuong Toan Tran, Ping-Lin Chang, Herbert De Praetere, Julies Maes, Dominiek Reynaerts, Jos Vander Sloten, Danail Stoyanov, and Emmanuel Vander Poorten, "3D Catheter Shape Reconstruction Using Electromagnetic and Image Sensors", Journal of Medical Robotics Research, Vol. 02, No. 03, 1740009 (2017), DOI: 10.1142/S2424905X17400098.

[20] Olympus bf-xp160f datasheet, https://pdf.medicalexpo.com/olympus-medicxp160f/69587-109253.html.

[21] Sonja Jäckle, Verónica García-Vázquez, Tim Eixmann, Florian Matysiak, Felix von Haxthausen, Malte Maria Sieren, Hinnerk Schulz-Hildebrandt, Gereon Hüttmann, Floris Ernst, Markus Kleemann & Torben Pätz, "Three-dimensional guidance including shape sensing of a stentgraft system for endovascular aneurysm repair", International Journal of Computer Assisted Radiology and Surgery, May 2020, Vol. 15, pp:1033–1042, DOI: 10.1007/s11548-020-02167-2.

[22] Arun KS, Huang TS, Blostein SD, "Least-squares fitting of two 3-D point sets ", IEEE Transactions on Pattern Analysis and Machine Intelligence, Sep. 1987, Vol.PAMI-9, pp: 698 - 700, DOI: 10.1109/TPAMI.1987.4767965.

[23] Michael D. Todd, Christopher J. Stull, Michael Dickerson, "A local material basis solution approach to reconstructing the three-dimensional displacement of rod-like structures from strain measurements", Journal of Applied Mechanics, Jul. 2013, Vol.80(4), DOI: 10.1115/1.4023023.

[24] Shuang Song; Zheng Li; Haoyong Yu; Hongliang Ren, "Electromagnetic Positioning for Tip Tracking and Shape Sensing of Flexible Robots", IEEE Sensors Journal, April 2015, Vol.: 15, pp: 4565 - 4575, DOI: 10.1109/JSEN.2015.2424228.

[25] LUNA Shape accuracy -Data-Sheet-ODiSI-6000-_v3.pdf.

[26] X. T. Ha et al., "Shape Sensing of Flexible Robots Based on Deep Learning," IEEE Transactions on Robotics, Vol. 39, No. 2, pp:1580-1593, April 2023, DOI: 10.1109/TRO.2022.3221368.